RSC Advances

PAPER

View Article Online
View Journal | View Issue

Cite this: *RSC Adv.*, 2020, **10**, 19431

Aqueous solution photocatalytic synthesis of *p*-anisaldehyde by using graphite-like carbon nitride photocatalysts obtained *via* the hard-templating route

Raquel A. Fernandes, Maria J. Sampaio, Joaquim L. Faria and Cláudia G. Silva *

Graphite-like carbon nitride (GCN)-based materials were developed *via* the hard-templating route, using dicyandiamide as the GCN precursor and silica templates. That resulted in urchin-like GCN (GCN-UL), 3D ordered macroporous GCN (GCN-OM) and mesoporous GCN (GCN-MP). The introduction of silica templates during GCN synthesis produced physical defects on its surface, as confirmed by SEM analysis, increasing their specific surface area. A high amount of nitrogen vacancies is present in modified catalysts (revealed by XPS measurements), which can be related to an increase in the reactive sites available to catalyse redox reactions. The textural and morphological modifications induced in GCN an enhanced light absorption capacity and reduced electron/hole recombination rate, contributing to its improved photocatalytic performance. In the photocatalytic conversion of *p*-anisyl alcohol to *p*-anisaldehyde in deoxygenated aqueous solutions under UV-LED irradiation, the GCN-UL was the best photocatalyst reaching 60% yield at 64% conversion for *p*-anisaldehyde production after 240 min of reaction. Under oxygenated conditions (air), the process efficiency was increased to 79% yield at 92% conversion only after 90 min reaction. The GCN-based photocatalyst kept its performance when using visible-LED radiation under air atmosphere. Trapping of photogenerated holes and radicals by selective scavengers showed that under deoxygenated conditions, holes played the primary role in the *p*-anisaldehyde synthesis. Under oxygenated conditions, the process is governed by the effect of reactive oxygen species, namely superoxide radicals, with a significant contribution from holes.

Received 25th March 2020
Accepted 11th May 2020

DOI: 10.1039/d0ra02746d

rsc.li/rsc-advances

Introduction

p-Anisaldehyde (or 4-methoxybenzaldehyde) is an aromatic aldehyde widely applied in food, beverages and pharmaceutical industries as a final product or as an intermediate to other reactions.[1,2] The industrial production of *p*-anisaldehyde usually involves the oxidation or methylation of *p*-cresol or anisole in organic solvents and hazardous conditions of temperature and pressure.[2] With the increasing demand for environmentally friendly synthetic routes that can lead to target organic products, the development of alternative and more ecological routes is a chief concern of society.

Heterogeneous photocatalysis presents itself as a greener alternative to the conventional hazardous processes adopted in the chemical industry. Besides allowing operation under mild conditions of temperature and pressure, the use of water as the solvent and eco-efficient sources of radiation (as light-emitting diodes, LEDs), allow a decrease in the environmental impact of the process, without compromising the selectivity and yield.[3]

Titanium dioxide (P-25 TiO_2) is the standard optical semiconductor widely used in several photocatalytic applications.[4] However, due to its low absorption in the visible range and its high application in several industrial areas, promoted the search for alternative semiconductors, as graphite-like carbon nitride-based materials (g–C_3N_4).

Graphite-like carbon nitride (here labelled as GCN) is a metal-free polymeric semiconductor constituted by tris-*s*-triazine units,[5,6] which possesses a bandgap (2.7 eV) narrower than that of the reference titanium dioxide (3.0–3.2 eV),[4] thus making it easily activated in a visible part of the electromagnetic spectrum, which represents a significant advantage concerning solar-driven processes.[5,6] GCN already proved to be a valid alternative to TiO_2 in several photocatalytic applications, as fine chemical synthesis,[7–9] hydrogen production[10–12] and degradation of pollutants.[5,13,14] However, the catalytic performance of this photocatalyst is negatively affected by its low surface area and high e^-/h^+ recombination rate, being necessary to adopt strategies to overcome these limitations.[8,15]

Laboratory of Separation and Reaction Engineering - Laboratory of Catalysis and Materials (LSRE-LCM), Faculdade de Engenharia, Universidade do Porto, Rua Dr Roberto Frias s/n, 4200-465, Porto, Portugal. E-mail: cgsilva@fe.up.pt

Templating routes have been applied for introducing morphological modifications in GCN.[16–23] With the use of soft and hard templates, physical properties as porosity, structure, morphology, surface area and size, can be tuned in order to improve the photocatalytic performance of the catalysts to a specific application.[24]

The novelty of the present work relies on the application of several GCN materials morphological modified by using silica templates to the photocatalytic organic synthesis. To the best of our knowledge, we present the first study reporting the impact of different morphological modifications of GCN on the photocatalytic synthesis of *p*-anisaldehyde (AAD) using highly efficient radiation sources (LEDs). The influence of oxygen in the yield of AAD was investigated, aiming at optimal conditions for upscale production. Finally, a reaction pathway was assessed by using scavengers to determine the active redox channels in the semiconductor.

Experimental

Materials

Dicyandiamide (DCN, 99%), hexadecyltrimethylammonium bromide (CTAB, 99%), polyvinylpyrrolidone K30 (PVP K30), hydrochloric acid (HCl, 37%), silicon dioxide (SBA-15, 99.6%), *p*-anisaldehyde (AAD, 98%), benzoquinone (BQ, 98%) and ethylenediaminetetraacetic acid (EDTA, ≥98%) were purchased from Sigma-Aldrich. Acetaldehyde (C_2H_4O, ≥99%), tetraethyl orthosilicate (TEOS, 99%) and formic acid (HCO_2H, 98%) were purchased from Fluka. Ammonium hydroxide (NH_4OH, 28%), *tert*-butanol (*t*-BuOH, 99%) and *p*-anisyl alcohol (AA, 98%) were purchased from Alfa Aesar. Sulfuric acid (H_2SO_4, 95–98%) was purchased from Labor and ethanol (CH_3CH_2OH, p. a.) was purchased from Panreac. Hydrofluoric acid (HF, 48%) and methanol (CH_3OH, 99.6%) were purchased by VWR™. Titanium dioxide (TiO_2) Aeroxide® P25 powder was supplied by Evonik and used as received. All the reagents were used without further purification. Ultra-pure water was obtained from a Direct-Q Millipore system.

Synthesis of morphologically modified GCN

The synthesis of bulk carbon nitride was performed by thermal decomposition of DCN as previously reported.[7] The precursor was heated at 2 °C min^{-1} up to 550 °C. The obtained solid was washed with deionized water to remove some precursor or impurities and dried overnight at 100 °C.

Morphologically modified GCN was obtained *via* the hard-templating route using three different methodologies, leading to materials with distinct properties. The resulting GCN-based materials were labelled as urchin-like GCN (GCN-UL), 3D ordered macroporous GCN (GCN-OM) and mesoporous GCN (GCN-MP).

The GCN-UL was synthesized according to the previously reported methodology.[22] Firstly, silica (SiO_2) template is prepared through the modified Stöber method.[25] This template was then mixed with dicyandiamide in a mass ratio of 1 : 1. The mixture was placed in a crucible and the same thermal treatment used for bulk GCN performed. The GCN-UL was washed several times with deionized water and dried at 100 °C overnight.

The GCN-OM was prepared as previously reported.[21] For the synthesis of the nanospheres, are necessary two solutions: (i) a solution containing 10 mL of TEOS in 50 mL of ethanol (solution A); and (ii) a water–ethanol solution (1 : 2) made of an aqueous solution of NH_4OH added to 50 mL of ethanol with vigorous stirring (solution B). Then, both solutions (A and B) are mixed and stirred at 40 °C for 2.5 h. After the treatment, a solution containing 10 mL of TEOS, 2 g of PVP K30 and 40 mL of ethanol was added dropwise with vigorous stirring and left at 40 °C for 2 h. Then, the mixture was left at room temperature overnight. Afterwards, the solution was centrifuged to align the structure and the solid dried at 100 °C. Lastly, the aligned SiO_2 solid was calcinated at 700 °C for 6 h to remove some residues of reagents. Finally, 0.8 g of SiO_2 nanospheres were pre-treated with 10 mL of 1 M HCl solution, then dried at 100 °C. Afterwards, 2 g of dicyandiamide was mixed with the pre-treated SiO_2 nanospheres and the mixture subjected to the heating program of GCN.

The synthesis of GCN-MP was performed by adding 2 g of dicyandiamide, 75 μL of concentrated sulfuric acid and 1 g of SBA-15 to a certain volume of deionized water.[23] The suspension was sonicated for 30 min and stirred at 70 °C for 6 h. After this, the mixture was filtered and dried at 100 °C to obtain a white solid. The white solid was placed in a crucible into the furnace and underwent the heating program of GCN. Finally, the material was washed with deionized water and dried at 100 °C.

All the GCN-based materials (GCN-UL, GCN-OM and GCN-MP) were post-treated with 4 M HF for 72 h to remove their specific template and dried at 100 °C.

Photocatalysts characterisation

The morphology of the materials was assessed by scanning electron microscopy (SEM) in a FEI Quanta 400 FEG ESEM/EDAX Genesis X4M (15 keV) instrument.

The elemental composition of the materials was determined through elemental analysis in a Carlo Erba EA 1108 Elemental Analyzer.

Fourier transform infrared (FTIR) measurements (4000–600 cm^{-1}) were performed on a JASCO FT/IR-6800 spectrometer (JASCO Analytical Instruments, USA) equipped with a MIRacle™ Single Reflection ATR (attenuated total reflectance ZnSe crystal plate) accessory (PIKE Technologies, USA). The analyses were performed using 256 scans with a resolution of 4 cm^{-1}.

The diffuse-reflectance UV-vis spectra (DR UV-vis) of the materials were conducted on a JASCO V-560 UV-vis spectrophotometer equipped with an integrating sphere attachment (JASCO ISV-469). The bandgap of the photocatalysts was determined from the respective Tauc plot.

The Brunauer–Emmett–Teller (BET) specific surface area (S_{BET}) was determined through the N_2 adsorption isotherm at −196 °C in the relative pressure range 0.05–0.20, using a Quantachrome NOVA 4200e apparatus.

Solid-state photoluminescence (PL) spectra were obtained at room temperature on a JASCO (FP 82000) fluorescence

spectrometer with a 150 W Xenon lamp as a light source using both excitation and emission bandwidth fixed at 2.5 nm. The excitation wavelength was set at 370 nm, and the emission was measured in the 380–650 nm range.

X-ray photoelectron spectroscopy analysis (XPS) was performed in a Kratos AXIS Ultra HAS equipment and Al monochromator operating at 15 kV (90 W) in hybrid mode. Binding energy values were referred to the C 1s peak at 284.4 eV. The obtained spectra were analysed and deconvoluted using the CasaXPS software.

Photocatalytic experiments

The photocatalytic efficiency of the GCN-UL, GCN-OM and GCN-MP materials was investigated in the synthesis of *p*-anisaldehyde (AAD) through the oxidation of *p*-anisyl alcohol (AA). The experiments were carried out in a circular glass reactor filled with 50.0 mL of 0.50 mM AA aqueous solution, at room temperature (20 °C) and without pH adjustment (*ca.* 5.4). The reactions were performed under oxygenated (air) and deoxygenated (argon) atmospheres. A dark period of 30 min was performed in order to establish the adsorption–desorption equilibrium. The photocatalytic experiments were performed under UV or visible light, using four-LED systems. The nominal average irradiance of UV and visible LEDs was 49.8 mW cm^{-2} and 45.0 mW cm^{-2}, respectively, was determined by using a UV-vis spectroradiometer (OceanOptics USB2000+). In a typical experiment, the suspension was irradiated for 4 h and samples were periodically withdrawn in order to evaluate the AA and AAD concentrations by High Performance Liquid Chromatography (HPLC), using a Shimadzu Corporation apparatus equipped with a Diode Array Detector (SPD M20A). A KinetexTM F5 1.7 μm 100 Å column (100 mm × 2.1 mm) was used with a solvent delivery pump (LC-30AD) at a flow rate fixed at 0.15 mL min^{-1}. The temperature of the column oven and autosampler were set at 35 °C and 4.0 °C, respectively. An equilibrated mixture of 0.1% v/v of formic acid (A) and methanol (B) with a ratio of 30 : 70 (A : B) was isocratically eluted for 20 min. The AA and AAD concentrations were determined at 226 nm and 282 nm, respectively.

According to the chemical stoichiometry, one molecule of AA can be oxidised to one molecule of AAD (1 : 1). The synthesis of AAD only starts when the radiation source is turned on, which means that the initial concentration of AAD is zero. The AA conversion (C), selectivity (S) and yield (Y) towards the AAD production are then defined as:

$$C\ (\%) = \frac{AA_0 - AA_t}{AA_0} \times 100$$

$$S\ (\%) = \frac{AAD_t - AAD_0}{AA_0 - AA_t} \times 100 = \frac{AAD_t}{AA_0 - AA_t} \times 100$$

$$Y\ (\%) = \frac{AAD_t - AAD_0}{AA_0} \times 100 = \frac{AAD_t}{AA_0} \times 100$$

in which, AA_0 is the initial concentration of AA (mM), AA_t is the concentration of AA (mM) at a given time t, and AAD_t is the concentration of AAD (mM) at a given time t. It is worth mentioning that following the adopted definitions, it results that $Y = C \times S$.

Photocatalytic experiments in the presence of scavengers (1.0 mM) for the hydroxyl radical (*t*-BuOH), superoxide radical (BQ) and holes (EDTA) were also performed to assess the photocatalytic reaction pathway.

Results and discussion

Characterisation of the templated GCN photocatalysts

Because we have previously characterised GCN and some GCN derivative materials,[7,10,11] in the following of this section we will provide new data on the materials specifically synthesized in the present study.

Using scanning electron microscopy (SEM) is possible to analyse the morphology of GCN and GCN-structured materials (Fig. 1).

As already reported, the compact structure of GCN (Fig. 1a) contributes to its low S_{BET} (7 m^2 g^{-1}), which may indicate a limited number of active sites.[7,26] The preparation of GCN-based catalysts through hard-templating has been reported as a route to change the morphology by increasing the surface area of the resulting materials.[20] We synthesized the GCN-MP, GCN-OM and GCN-UL materials by using three different templates of SiO_2, respectively, the commercial mesostructured silica (SBA-15), core–shell SiO_2 nanospheres and flower-like SiO_2 nanoparticles. The introduction of these templates in the process of synthesis of GCN induced a change on its morphology. In the case of GCN-MP, it is possible to observe a multilayer stacking structure (Fig. 1b), similar to the morphology of bulk GCN. Yet, some induced defects are also detected, which may indicate a mesoporous structure. In terms of S_{BET}, the results revealed an increase of 57% (11 m^2 g^{-1}) when compared to bulk GCN. Regarding GCN-OM, the introduction of SiO_2 nanospheres led to the detection of well-defined macropores on its surface, which are distinguishable in Fig. 1c. The induction of physical defects on the surface of a photocatalyst may enhance the photocatalytic performance by increasing its S_{BET}[13,18,21,22,25] (20 m^2 g^{-1}) as occurred in the case of the GCN-OM material. In the case of GCN-UL, the particles are smaller (Fig. 1d), which is in line with an increase in the S_{BET} (28 m^2 g^{-1}).

Besides, from SEM micrographs is also possible to infer that the morphological modifications occurred mainly on the surface of the catalysts, reinforcing the impact of hard-templating in the surface area of GCN, which was enhanced by the following order GCN (7 m^2 g^{-1}) < GCN-MP (11 m^2 g^{-1}) < GCN-OM (20 m^2 g^{-1}) < GCN-UL (28 m^2 g^{-1}).

The similarity of the FTIR-ATR spectra (data not shown) confirms that the base structure of the GCN materials is kept. The presence of an IR band at 3000–3250 cm^{-1} is due to the N–H and N–H_2 stretching vibrations of primary and secondary amines.[7,21–23] The band at 1500–1700 cm^{-1}, is characteristic of the C–N stretching vibrations, while the 1200–1400 cm^{-1} band represents the aromatic C–N stretching. The sharp peak identifies the CN heterocycles of the triazine ring at around 800 cm^{-1}.[7,21–23]

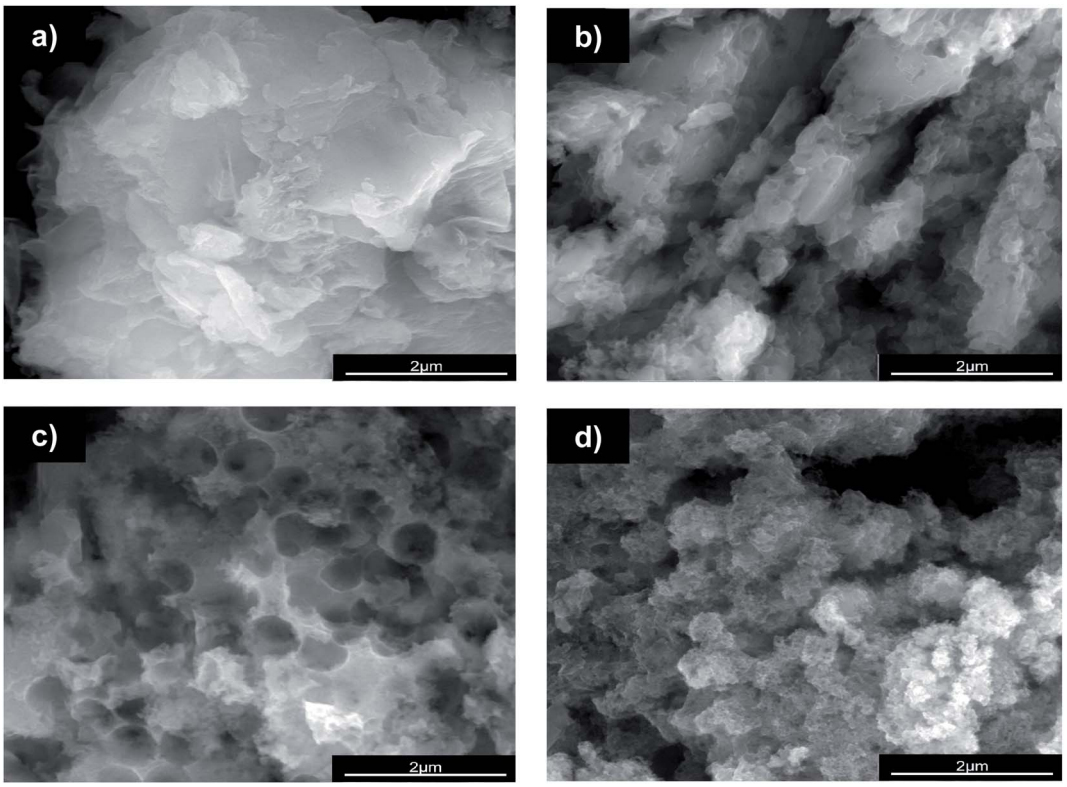

Fig. 1 SEM micrographs of (a) GCN, (b) GCN-MP, (c) GCN-OM and (d) GCN-UL.

Analysis of the XPS spectra provided information on the elemental composition of the prepared materials (Fig. 2).

The C 1s XPS spectra of GCN and GCN-based catalysts (Fig. 2a) shows how the binding energy of the carbon depends on the type of hybridization and nature of the carbon as we obtained 4 main peaks (C1, C2, C3 and C4) in the deconvolution of the individual spectrum. The C 1s binding energy at 284.4 eV (C1) is generally attributed to the impurity carbon, as in graphitic domains.[27–30] The binding energy at 286.0 eV (C2) is ascribed to sp^3-bonded defects on the GCN surface due to the amino functional groups (C–NH_2).[7,18] The dominant C3 peak located at 288.0 eV is assigned to the presence of sp^2-hybridized C atoms in N-containing aromatic rings (N–C=N).[7,18,22] Between 293.0 and 294.0 eV is located the C4 peak, which is related to the π electron delocalization in melon heterocycles.[19,22,31]

Concerning the N 1s XPS spectra (Fig. 2b), it is possible to isolate 4 different binding energies (N1, N2, N3 and N4). The N 1s energy of 398.6 eV (N1) is generally ascribed to the sp^2-bonded nitrogen involved in triazine rings (C–N=C).[20,22] The binding energy of 399.4 eV (N2) is attributed to the presence of tertiary N in N–$(C)_3$ structures, which corroborates the effective polymerization of dicyandiamide into GCN.[20,22] The N3 peak located at 400.4 eV is related to the presence of heptazine units, with –NH and –NH_2 groups.[7,20] The relocation of positive charges in melon heterocycles and cyano groups is confirmed through the N4 peak at 404.4 eV.[7,18]

The XPS analysis confirms the previous FTIR-ATR results, showing that the incorporation of SiO_2 templates in the process of synthesis did not induce any chemical modification of GCN, with no additional element identified in the survey (data not shown).

However, there are significant differences in the amounts of each of the extracted binding energies of the N 1s XPS spectra concerning the GCN-UL and GCN samples. The ratio between N1 and N2 binding energies expresses the presence of structural defects applied to the C–N plane, due to the presence of nitrogen vacancies that promote the conversion of C–N=C into N–$(C)_3$.[10,32–35] The N1/N2 peak ratio follows the order GCN > GCN-MP > GCN-OM > GCN-UL (1.74, 1.42, 1.40 and 0.75, respectively). The observed decrease indicates the presence of nitrogen vacancies at sp^2-bonded nitrogen (N1) in the modified catalysts. It is the GCN-UL that presents the lowest ratio, which indicates the highest nitrogen loss at the N1 site. Additionally, the modified catalysts present also the highest contribution of N2 peak and lower of N1 peak, being GCN-UL the catalyst with the highest and lowest value, respectively (Fig. 2). These observations indicate that GCN-UL presents a higher density of nitrogen-vacancy defects than the other modified catalysts.[32–35]

By DR UV-vis and PL spectroscopies, we assessed the electronic properties of GCN-based materials. The bulk GCN presents a characteristic high absorption band in the visible spectral region (λ < 450 nm, Fig. 3a) corresponding to the bandgap transition.[7] The spectrum of GCN-MP is very similar to that of bulk GCN. In the case of GCN-OM and GCN-UP, the low wavelength resolution is lost. However, new important features are visible in their spectra. For GCN-OM there is a significant blue

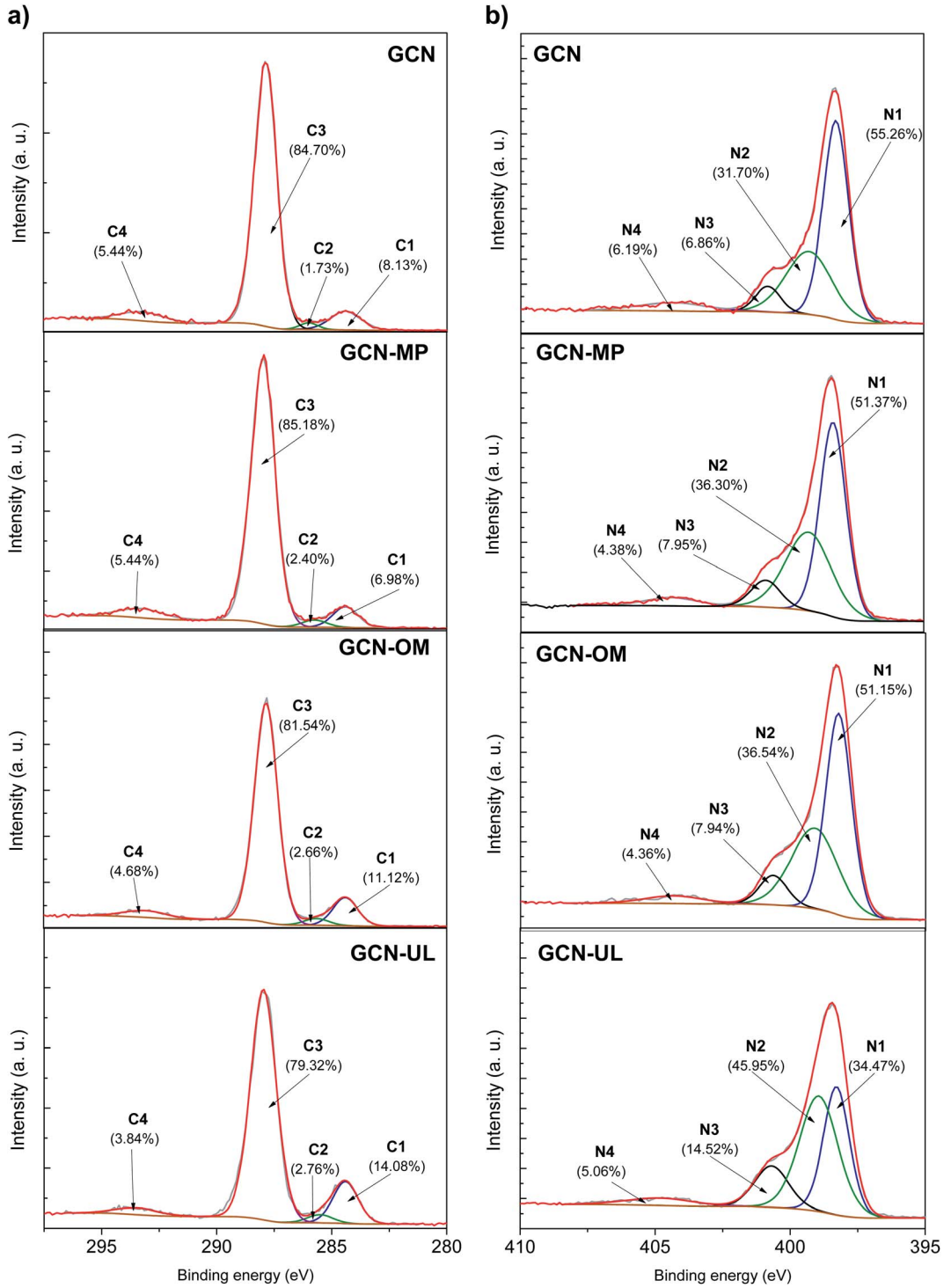

Fig. 2 (a) C 1s and (b) N 1s XPS spectra of GCN, GCN-MP, GCN-OM and GCN-UL.

shift of the spectrum, that will influence the bandgap of this photocatalyst. On the other hand, for GCN-UL there is a tail absorption that extends to the visible part of the spectrum.

The bandgap energies (E_g) for each of the photocatalysts was determined by the corresponding Tauc plot (inset Fig. 3a). The GCN bulk holds a bandgap energy of 2.86 eV, which is in agreement with the literature.[7,24,36] A similar bandgap was observed for GCN-MP (E_g = 2.88 eV), while a shift towards higher values of E_g was observed for GCN-OM and GCN-UL (2.99 and 3.00 eV, respectively).

The PL spectra of bulk GCN and the GCN-based materials (Fig. 3b) were obtained at room temperature with excitation at 370 nm. As shown, the incorporation of SiO_2 templates decreases the luminescence intensity of the photocatalysts.

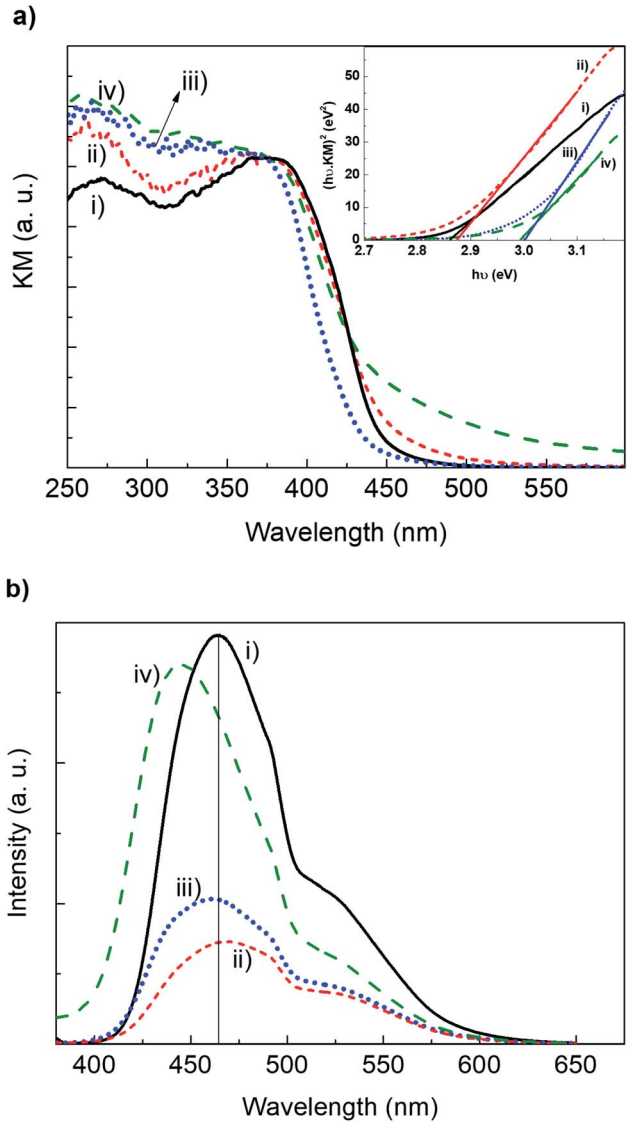

Fig. 3 (a) DR UV-vis spectra (inset shows the respective Tauc plot) and (b) solid state PL spectra of (i) bulk GCN, (ii) GCN-MP, (iii) GCN-OM and (iv) GCN-UL.

The high luminescence intensity of GCN materials is usually related to the high recombination rate between the photogenerated e^-/h^+ pairs, which can be due to the inefficient separation between these charge carriers, leading to low activities in photocatalytic applications.[37] The quenching detected in the emission of light in the form of luminescence of GCN-UL, GCN-MP and GCN-OM may indicate an improved e^-/h^+ separation efficiency and an extended charge carrier lifetime.[38] Another important aspect concerning the PL spectra of the synthesized materials is the wavelength of maximum intensity peak. In the case of GCN, the maximum of luminescence occurs at 468 nm (Fig. 3b). A shift to lower wavelengths occurred to GCN-UL and GCN-OM (444 and 461 nm, respectively), and a slight shift to higher wavelengths (489 nm) was verified in the case of GCN-MP (Fig. 3b).

Photocatalytic results

The designed photocatalysts were used in the controlled oxidation of *p*-anisyl alcohol (AA) to *p*-anisaldehyde (AAD) in aqueous solution using LED light sources.

Generally, the synthesis of aldehydes from the corresponding alcohols is performed under air saturation, once the presence of dissolved oxygen in the reaction medium allows the generation of reactive oxygen species (ROS), which have a substantial contribution to the oxidative pathway.[39] However, the oxidation of alcohols by ROS is a highly unselective route, leading to the production of side-products and reducing the selectivity of the photocatalytic process. Working under an inert atmosphere, using argon or nitrogen, limits the oxidation to the photogenerated holes, forcing it to the valence band of the semiconductor as we demonstrated in a previous work.[8]

Using the GCN-based photocatalysts, the synthesis of AAD in the absence of oxygen, performed with exciting conversions and yields (Fig. 4). The morphological modifications produced in the GCN surface promote not only an increase in the AA conversion rate (Fig. 4a) but also an enhancement in the yield of AAD (Fig. 4b), compared to the bulk GCN material.

The bulk GCN reached 20% of AA conversion, while the modified materials (GCN-MP, GCN-OM and GCN-UL) achieved 36%, 44% and 64% of *C*, respectively (Fig. 4c) after 240 min of reaction. In terms of AAD synthesis, was found a maximum concentration of 0.08 mM after 240 min of reaction with the bulk GCN material (Fig. 4b). Concerning the GCN-based materials, the concentration of AAD duplicated to GCN-MP (0.15 mM) and triplicated to GCN-OM and GCN-UL (0.27 mM) in the same reaction time (Fig. 4b). According to the results obtained both in AA oxidation and in AAD production, the photocatalytic performance of GCN-based catalysts increases by the following order: GCN < GCN-MP < GCN-OM < GCN-UL. This relation was also observed in the surface area value (Section 3.1.). It is well established in the literature that in heterogeneous photocatalytic processes the specific surface area can significantly affect the efficiency of the catalysts, with a highly defective surface area resulting in a higher surface area and, consequently, in more active sites available for reactivity between the molecules and the catalyst surface.[18,20–23,40] As previously discussed, the morphological modifications induced on the surface of GCN-based catalysts led to an increase in their S_{BET}. The defects introduced on the surface of the catalysts (as confirmed by SEM analyses, Fig. 1) can act as active sites, enhancing the oxidation of organics, while the reduced particle size maximizes the surface contact ratio, which usually leads to more efficient systems.[22] Correspondingly, the presence of these defects enhances the performance of the photocatalysts, by acting as active centres for the photogeneration of e^- and h^+ in the conduction and valence bands, respectively.[10,32,33,35]

By introducing surface modifications, the yield (*Y*) increases from 18% (GCN) to 32% (GCN-MP), 42% (GCN-OM) and 60% (GCN-UL) over 4 h reaction (Fig. 4c).

The higher efficiency of GCN-based materials seems to indicate that the morphological and textural properties are responsible for the enhancement of the GCN-based materials

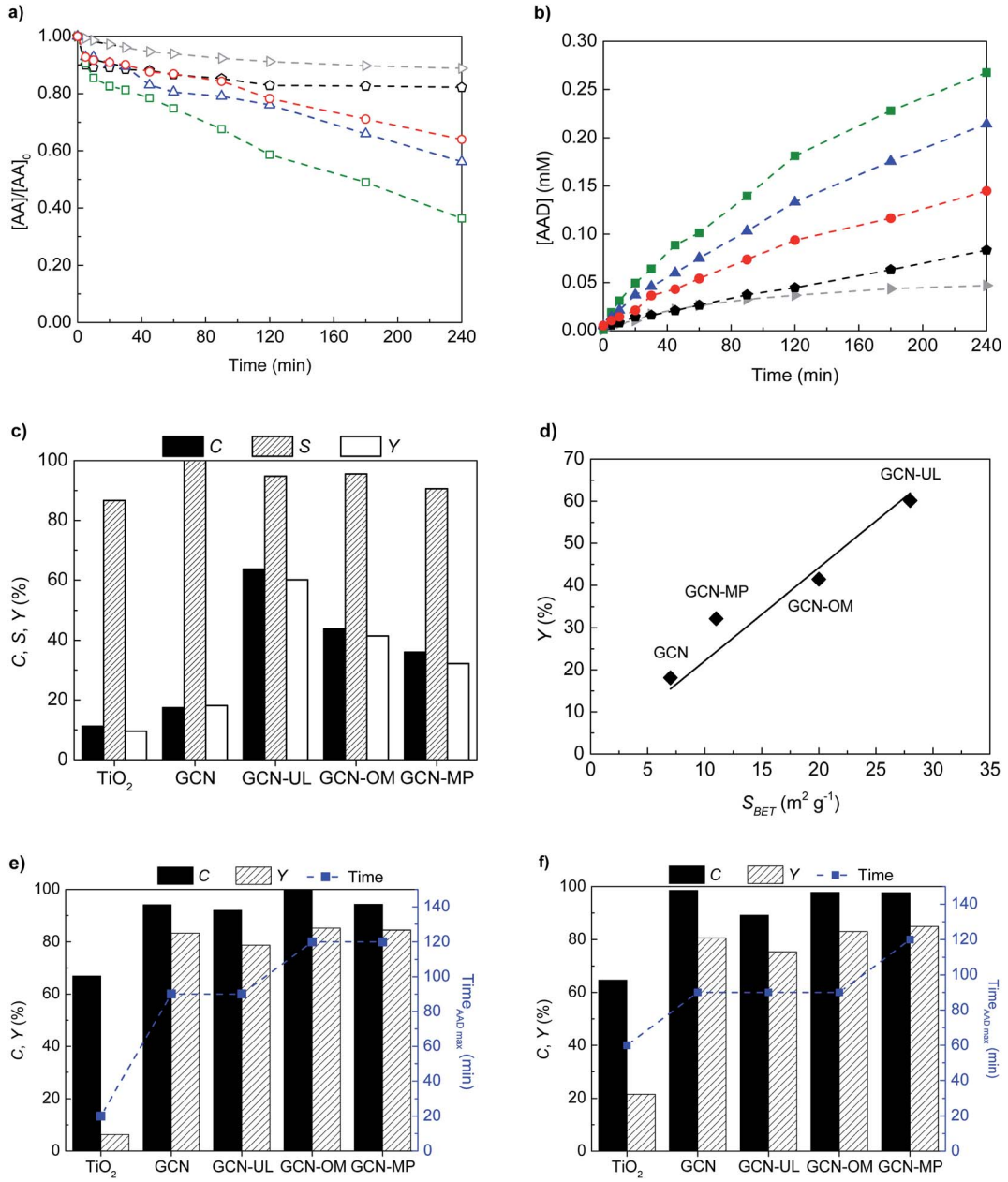

Fig. 4 (a) Normalized concentration of AA and (b) AAD using GCN (⬠, ⬟), GCN-MP (○, ●), GCN-OM (△, ▲), GCN-UL (□, ■) and TiO_2 (▷, ▶) after 240 min reaction under deoxygenated conditions. (c) *C*, *S* and *Y* using the photocatalysts under deoxygenated conditions. (d) Effect of S_{BET} in the photocatalytic performance of all catalysts. Solid line represents the linear fitting ($r^2 > 0.98$). Reaction time of maximum AAD concentration (■) and the respective values of *C* and *Y*, using the GCN-based photocatalysts under oxygenated conditions, using UV-LED (e) and visible-LED (f) radiation.

for AAD production. In fact, the relation between the S_{BET} of GCN-based materials and their photocatalytic performance on the production of AAD seems to be linear, with the increase of *Y* with the increase in S_{BET} (Fig. 4d). Moreover, the higher amount of nitrogen vacancies detected by XPS analysis can also contribute to the activity enhancement of these photocatalysts, due to electron relocation.[41]

Since for field applications working under air is preferable, the catalysts were tested under those conditions (Fig. 4e). Not surprisingly, the conversion of AA increased in the presence of oxygen, achieving more than 95% of *C* after 120 min of reaction for all GCN-based catalysts (Fig. 4e). The increase in the conversion of AA combined with the high selectivity (above 80%) for the GCN-based catalysts significantly increases the yield of the photocatalytic production of AAD under air saturation (Fig. 4e). Owing to the presence of oxygen the peak for AAD yield was reached at significantly reduced reaction times (between 90 and 120 min, Fig. 4e), compared with that under an argon atmosphere, in which the production of AAD was continuously increasing over 240 min of reaction (Fig. 4b).

Table 1 Published works on the photoconversion of anisyl alcohol (AA) into *p*-anisaldehyde (AAD)

Entry	Catalyst	Radiation source	Power (W)	*V* (mL)	Gas	*t* (h)	*C* (%)	*Y* (%)	Energy efficiency,[b] (*E*)	Ref.
1	Anatase TiO_2	Hg lamp	125	500	O_2	7.7	65	42	0.218	47
2	Rutile TiO_2	Hg lamp	125	500	O_2	2.36	50	30	0.508	48
3	Rutile TiO_2	Hg lamp	450	500	O_2	8.8	50	31	3.91×10^{-2}	49
4	Brookite TiO_2	Hg lamp	125	500	O_2	2.1	50	12	0.229	50
5	Brookite TiO_2	UV fluorescent lamp	45	150	Air	4	40	12	0.100	51
6	TiO_2	UV fluorescent lamp	45	150	Air	2.3	20	18	0.261	52
7[a]	Pt/TiO_2	Xenon lamp	n. i.	n. i.	N_2	3	56	56	n. d.	53
8	F-doped TiO_2	UV fluorescent lamp	45	150	Air	4	23	13	0.108	54
9	N-doped TiO_2	Solar light simulator	1500	150	O_2	1	10	9	9.00×10^{-3}	55
10	TiO_2–graphene	Xenon lamp	300	1.5	O_2	20	70	70	1.75×10^{-4}	56
11	WO_3/TiO_2	Hg lamp	450	5	O_2	6	50	32	5.93×10^{-4}	57
12	TiO_2/Ag/DIOL	UV fluorescent lamp	45	150	Air	4	54	46	0.383	58
13	Ag_3PO_4	Solar light simulator	230	130	Air	2	>85	84	0.237	59
14	Pt/nanoporous Bi_2WO_6	Tungsten-halogen lamp	230	130	Air	4	>95	>94	0.133	60
15	CdS	Xenon lamp	300	20	O_2	3	25	15	3.33×10^{-3}	9
16	N-doped g–C_3N_4	Xenon lamp	300	10	O_2	9	86	9	3.33×10^{-4}	41
17	P-doped g–C_3N_4	Halogen lamp	100	150	O_2	4	100	72	0.270	61
18	mpg-CN	Xenon lamp	300	20	O_2	3	56	50	1.11×10^{-2}	9
19	**GCN-UL**	**UV-LED**	**40**	**50**	**Argon**	**4**	**64**	**61**	**0.191**	**Present**
20	**GCN-UL**	**UV-LED**	**40**	**50**	**Air**	**1.5**	**92**	**78**	**0.650**	**study**
21	**GCN-UL**	**Vis-LED**	**40**	**50**	**Air**	**1.5**	**89**	**75**	**0.625**	

[a] n. i. – not indicated; n. d. – not determined. [b] Units of *E*: mol_{AAD} mL $mol^{-1}{}_{AA_0}$ W^{-1} h^{-1}.

The results under oxygenated conditions can be ascribed to the highly oxidative capacity of the generated ROS, such as hydroxyl and superoxide radicals, when compared to the photogenerated h^+. Depending on the photocatalysts properties and reaction conditions, when ROS are present in the medium, the oxidation of organic compounds seem to be widely enhanced,[41] and thus h^+ acting as a secondary oxidative route. Thus, the presence of oxygenated species on the reaction medium for AAD production seems to hide the positive impact of the morphological and textural modifications in the photocatalytic performance of GCN-based materials.

One of the most attractive characteristics of GCN-based materials is their ability to absorb light in the visible range, unlike P-25 TiO_2.[3] Following the results obtained under air in the UV, the efficiency of GCN-based catalysts was evaluated under air atmosphere but using four visible LEDs emitting at 417 nm (Fig. 4f).

The photocatalytic synthesis of AAD through the oxidation of AA under visible light irradiation kept the higher values of *C* and *Y*, reaching more than 90% and 75%, respectively for all GCN-based materials (Fig. 4f), without compromising selectivity (>80%). The SiO_2 templates incorporated during their synthesis procedure of structured GCN catalysts promote multiple scattering and slow photon effects, responsible for improving inner light reflection.[22,23,42,43] As displayed in Fig. 4a–c and 4e, the commercial TiO_2 P25 exhibit lower efficiency than the GCN-based catalysts, presenting lower AA conversion and lower selectivity to AAD under the same experimental conditions (λ_{exc} = 370 nm). Besides, under visible light irradiation (λ_{exc} = 417 nm; Fig. 4f), the TiO_2 P25 also showed much lower efficiency for AA conversion, which was already expected since TiO_2 presents residual visible-light absorption capacity.

Table 1 compiles the published works on the photocatalytic synthesis of AAD by selective oxidation of AA. TiO_2-based catalysts are the most applied materials (Table 1, entries 1–12). Alternative methodologies were adopted to improve TiO_2-based catalysts performance, such as metal- and elemental-doping approach (Table 1, entries 7–9), the formation of heterojunctions with other catalysts (Table 1, entries 10–12). By using metallic catalysts, namely Ag_3PO_4 (Table 1, entry 13) and Pt/nanoporous Bi_2WO_6 (Table 1, entry 14), high yields were achieved (>80%). However, this type of catalysts has a profoundly negative impact over environmental sustainability by opposition to metal-free catalysts, as carbon nitride (Table 1, entries 16–18). Opposing the modest yields (9%) obtained for N-doped g–C_3N_4 (Table 1, entry 16) are the more effective P-doped g–C_3N_4 (Table 1, entry 17) and mpg-CN (Table 1, entry 18) photocatalysts.

Considering the catalysts produced in this study, GCN-UL reached 61% of *Y* and 64% of *C* after 4 h reaction (Table 1, entry 19) under UV-LED irradiation in the absence of oxygen. By introducing air (Table 1, entries 20 and 21), GCN-UL reached higher values of *C* and *Y* (>89% and >75%, respectively) at very reduced reaction times (1.5 h), using either UV- or vis-LED radiation (Table 1, entries 13 and 14), overall surpassing the performance of the compiled photocatalysts.

Another critical aspect of the photocatalytic processes is the type of radiation source. Through the analysis of Table 1, the photocatalytic conversion of AA to AAD was mainly driven by conventional light sources, like xenon, fluorescent and halogen lamps. Contrariwise to the conventional lamps, LEDs offer high

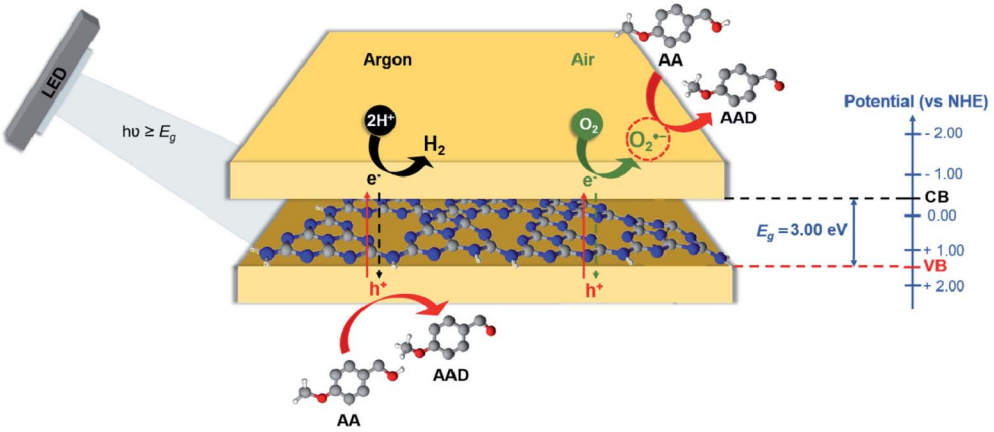

Scheme 1 Diagram of photocatalytic conversion of AA into AAD under deoxygenated and oxygenated conditions, using GCN-UL as photocatalyst and UV-LED as light source.

energy efficiency, with longer lifetime and higher flexibility to the reactor design.[44–46] We defined an energy efficiency parameter (E) in terms of the moles of AAD produced, times volume, per mole of initial AA, per watt, per hour, to compare the compiled processes (Table 1) as follows:

$$E = \frac{Y \times V}{P \times t} = \frac{[\mathrm{AAD}] \times V}{[\mathrm{AA}]_0 \times P \times t}$$

in which Y is the yield toward to AAD synthesis ([AAD] and $[AA]_0$ are the molar concentration of *p*-anisaldehyde at given time and the initial molar concentration of anisyl alcohol, respectively), V is the reaction volume (mL), P is the power of the radiation source (in W), and t is the irradiation time (h).

Our results with GCN-UL provide efficiency in excess of 0.625 mL W^{-1} h^{-1} in terms of mol of AAD per initial mol of AA. This result directly bounds with the improved photocatalytic performance of the photocatalyst and the low energetic demand of the light source. In this sense, the present work represents a technological breakthrough in the ecological impact of the photoconversion as means of converting AA into AAD.

Reaction pathway

Based on the described results, it is clear that the photocatalytic oxidative synthesis of AAD from AA depends on the reduction/oxidation properties of the templated GCN materials. The reaction can either proceed by the oxidative channel of the photocatalyst, using the photogenerated holes as oxidation agent or through the reductive channel, using reactive oxygen species (ROS) generated in the conduction band as the oxidation agent (Scheme 1).

To investigate either possibility, we used GCN-UL as probe photocatalyst under UV-LED illumination (Fig. 5).

Because of the nature of the photocatalyst, the participation of HO$^{\bullet}$ radicals as oxidative ROS species is expected to be irrelevant.[62] The addition of *t*-BuOH did not change the conversion and selectivity of the reaction significantly (Fig. 5). We observed a slight decrease in the rate as the time for conversion increased somewhat.

Adding EDTA (an h^+ scavenger) the effect on the final conversion and selectivity was similar to that of *t*-BuOH, however, the rate was decreased by more than two times as the time for final conversion went from 90 to 180 min. It follows that there is an apparent dependency on the heterogeneous conversion of AA by the photogenerated holes of the GCN-UL photocatalyst.

Finally, in the presence of benzoquinone (BQ, an $O_2^{\bullet-}$ scavenger) the reaction was significantly slowed down: it took 240 min to reach a little over 20% conversion.

Despite the oxidative channel of the GCN being important, there is no doubt that the $O_2^{\bullet-}$ radicals are determinant to the reaction mechanism. Scavenging the holes (with EDTA) in the absence of oxygen (therefore no $O_2^{\bullet-}$, thus a double scavenging experiment) leads to a result similar to the one obtained in the presence of BQ (Fig. 5).

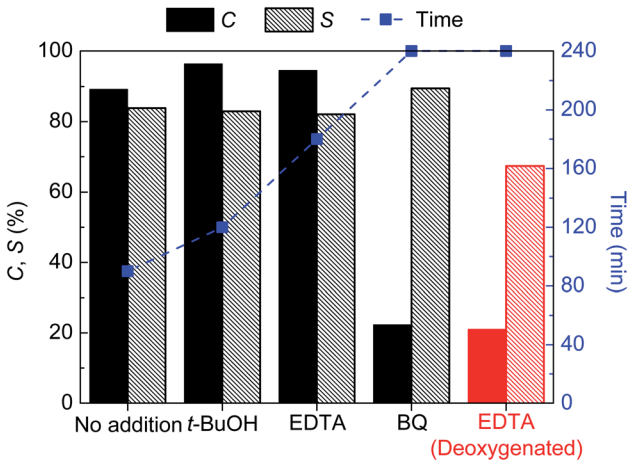

Fig. 5 Effect of scavengers in the photocatalytic performance of GCN-UL under air (black columns) and argon (red columns) atmospheres, using a UV-LED radiation source. The *C* and *S* values are determined to the maximum of AAD production, with the indication of the respective reaction time (■).

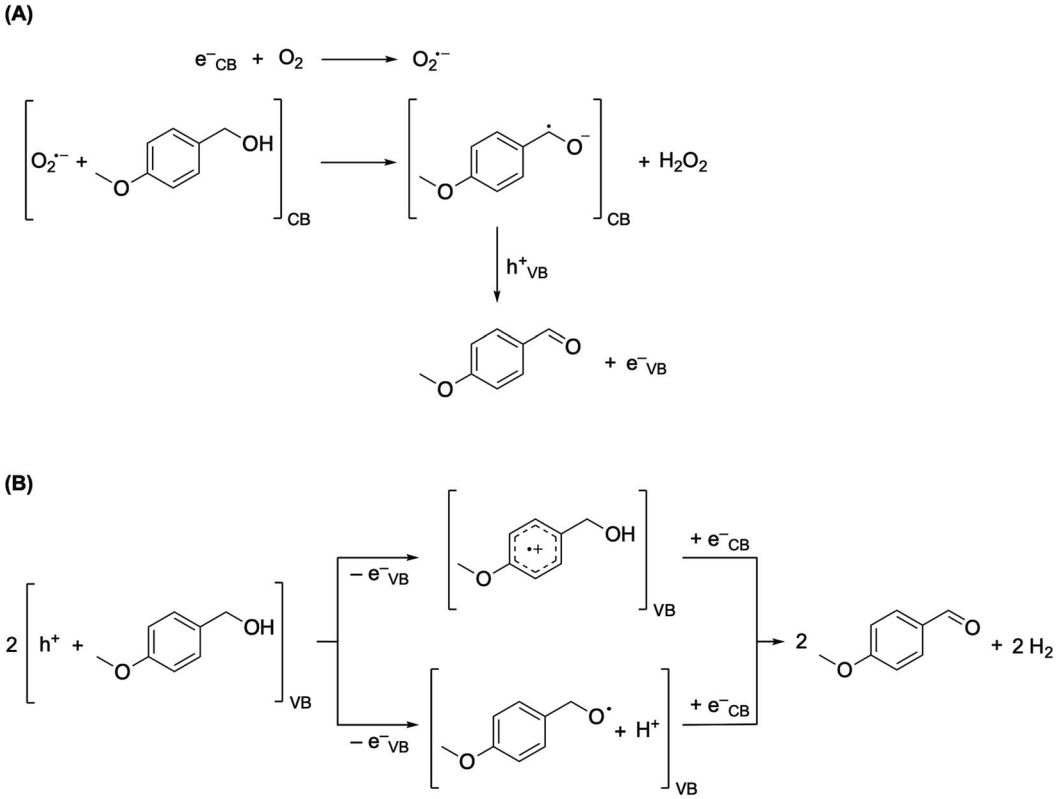

Fig. 6 Possible reaction mechanism for the equilibrated photocatalytic cycle of AA selective oxidation to AAD over the GCN-UL photocatalyst, starting at the reductive channel (A) or, in alternative, at the oxidative channel (B).

The photocatalytic synthesis of aromatic aldehydes both in the presence and absence of oxygenated species is already mentioned in the literature.[6,41,63–65] Our observations confirm those reports and can be outlined by the proposed mechanism (Fig. 6).

The photocatalytic synthesis of alcohols described in literature is mainly concerned with TiO_2-assisted photocatalysis, following basically two mechanisms: direct oxidation by photogenerated holes or bulk oxidation through HO$^\bullet$ radical.[66] Due to the nature of our catalyst and the reported scavenging experiments, the involvement of the HO$^\bullet$ radical is ruled out. We are left to the direct oxidation by the photogenerated holes on the GCN-UL (Fig. 6B), and to the indirect oxidative H_2O_2 elimination by the superoxide radical anion $O_2^{\bullet-}$ (Fig. 6A).

The photogenerated excited electron e^- occurring at the conduction band reacts with the adsorbed molecular oxygen O_2, to generate the $O_2^{\bullet-}$ which in the presence of the AA produces a charge separated dehydrogenated radical anion of the AA and hydrogen peroxide H_2O_2. Oxidative electron transfer to the photogenerated hole of the valence band of GCN-UL results in the corresponding AAD formation (Fig. 6A).

Oxidation of the adsorbed AA molecule directly on the photogenerated holes at the valence band of the GCN UL leads to any of two, the formation of the AA radical cation, or the deprotonated AA radical (Fig. 6B). Either oxidised species adsorbed over the photoexcited GCN UL will accept back an electron to produce the ADD and molecular hydrogen (Fig. 6B).

Each of the pathways is a very beautiful example of a closed path oxidation/reduction mechanism, or *vice versa*, occurring on the surface of the photoexcited GCN-UL photocatalyst. The driving force for such an efficient process is the natural recombination of the photogenerated electrons and holes. That steep kinetic control also provides the means to the controlled reaction, preventing further oxidation the corresponding carboxylic acid.

In general, for these GCN materials, we can disguise two operative pathways: one prevalent in deoxygenated conditions, which runs effectively through the oxidative channel were AAD is mostly produced directly through the photogenerated holes; the other is running on the reductive channel, in the presence of molecular oxygen (air conditions), using the effectively generated $O_2^{\bullet-}$ by indirect oxidation in the conduction band (Scheme 1). Briefly, upon UV-LED illumination ($\lambda_{exc} = 370$ nm), photogenerated e^-/h^+ pairs occur in the surface of the GCN-UL, providing the redox channels for the reactions. In the absence of oxygen, h^+ in the valence band (VB) is the only responsible for the conversion of AA. Under these conditions, the photogenerated e^- in the conduction band (CB) leads to the reduction of H^+ to H_2.

On the other hand, in the presence of oxygen, the photogenerated e^- in the conduction band (CB) leads to the formation of $O_2^{\bullet-}$ radicals (a ROS). These radical species, together with the photogenerated h^+ on the VB, seems to play the leading role on the high efficiency for AAD production under oxygenated conditions.

Conclusions

Graphite like carbon nitride (GCN)-based photocatalysts with morphological and textural modifications were obtained using SiO_2, through the hard-templating technique.

The photocatalysts were thoroughly characterised and tested in the photocatalytic synthesis of *p*-anisaldehyde by the oxidation of anisyl alcohol. Despite the conditions necessary, it is clear that the structural triazine units of the GCN are strong enough to keep their integrity during the process. Although the triazine planes of carbon nitride are maintained, there is no way to confirm the graphitic nature of the interaction between the sheets. This fact is no impeditive of obtaining materials with good photocatalytic performances.

The impact of the morphological constraints in the photocatalytic performance was notorious when compared to the other photocatalysts in the existing literature.

The pathway here proposed for AAD production demonstrates the importance of considering different contributions from the oxidative and reductive channels of the organic semiconductor photocatalyst.

Because the materials are organic semiconductors, their variable behaviour may indicate that there is a difference between the optical bandgap and the transport gap (electrical bandgap), playing a role in photocatalytic performance.

Nevertheless, the results obtained at different activation wavelengths in the electromagnetic spectrum, confirm the enormous ability of these materials to operate under open-air solar conditions. It does not preclude the need to study all operation reaction parameters involved in the process, including atmosphere medium conditions, light sources, pH, initial concentration, temperature, among others if aiming at commercial application.

The present study adds the technique of hard-templating to the portfolio of assembly of GCN-based materials with high potential in heterogeneous photocatalysis, as an alternative to the conventional synthesis of value-added products, as *p*-anisaldehyde. Moreover, the metal-free character of the catalysts, the use of aqueous solutions, the low-cost and efficient radiation sources (UV- or visible-LED) are all positive aspects compared to the conventional organic synthesis processes.

Conflicts of interest

There are no conflicts to declare.

Acknowledgements

This work was financially supported by the base funding of the Associate Laboratory LSRE-LCM (UIDB/50020/2020), financed by national funds through FCT/MCTES (PIDDAC), and by the Projects POCI-01-0145-FEDER-030674 and POCI-01-0145-FEDER-031398 funded by ERDF through COMPETE2020 – Programa Operacional Competitividade e Internacionalização (POCI) – and by national funds through FCT – Fundação para a Ciência e a Tecnologia. R. A. F. acknowledges the PhD fellowship funded by Project NORTE-08-5369-FSE-000028, supported by Norte Portugal Regional Operational Programme (NORTE 2020), under the PORTUGAL 2020 Partnership Agreement, through the European Social Fund (ESF). C. G. S. acknowledges the FCT Investigator Programme (IF/00514/2014) with financing from the ESF and the Human Potential Operational Programme. We are indebted to Dr Carlos Sá and the CEMUP team (Portugal) for technical assistance and advice with SEM and XPS measurements.

Notes and references

1 K.-G. Fahlbusch, F.-J. Hammerschmidt, J. Panten, W. Pickenhagen, D. Schatkowski, K. Bauer, D. Garbe and H. Surburg, in *Ullmann's Encyclopedia of Industrial Chemistry*, Wiley-VCH Verlag GmbH & Co. KGaA, Weinheim, Germany, 2012, pp. 74–198.
2 A. K. Mukhopadhyay, Derivatives of Para-Cresol, in *Industrial Chemical Cresols and Downstream Derivatives*, M. Dekker, Taylor & Francis, New York, 2004, pp. 63–96.
3 D. Friedmann, A. Hakki, H. Kim, W. Choi and D. Bahnemann, *Green Chem.*, 2016, **18**, 5391–5411.
4 K. Nakata and A. Fujishima, *J. Photochem. Photobiol., C*, 2012, **13**, 169–189.
5 L. Svoboda, P. Praus, M. J. Lima, M. J. Sampaio, D. Matýsek, M. Ritz, R. Dvorský, J. L. Faria and C. G. Silva, *Mater. Res. Bull.*, 2018, **100**, 322–332.
6 G. Marcì, E. I. García-López and L. Palmisano, *Catal. Today*, 2018, **315**, 126–137.
7 M. J. Lima, A. M. T. Silva, C. G. Silva and J. L. Faria, *J. Catal.*, 2017, **353**, 44–53.
8 M. J. Lima, P. B. Tavares, A. M. T. Silva, C. G. Silva and J. L. Faria, *Catal. Today*, 2017, **287**, 70–77.
9 B. Long, Z. Ding and X. Wang, *ChemSusChem*, 2013, **6**, 2074–2078.
10 E. S. Da Silva, N. M. M. Moura, A. Coutinho, G. Dražić, B. M. S. Teixeira, N. A. Sobolev, C. G. Silva, M. G. P. M. S. Neves, M. Prieto and J. L. Faria, *ChemSusChem*, 2018, **11**, 2681–2694.
11 E. S. Da Silva, N. M. M. Moura, M. G. P. M. S. Neves, A. Coutinho, M. Prieto, C. G. Silva and J. L. Faria, *Appl. Catal., B*, 2018, **221**, 56–69.
12 X. Wang, K. Maeda, A. Thomas, K. Takanabe, G. Xin, J. M. Carlsson, K. Domen and M. Antonietti, *Nat. Mater.*, 2008, **8**, 76.
13 Y. Cui, J. Huang, X. Fu and X. Wang, *Catal. Sci. Technol.*, 2012, **2**, 1396–1402.
14 J. Mao, L. Zhang, H. Wang, Q. Zhang, W. Zhang and P. Li, *Chem. Eng. J.*, 2018, **342**, 30–40.
15 J. Kou, C. Lu, J. Wang, Y. Chen, Z. Xu and R. S. Varma, *Chem. Rev.*, 2017, **117**, 1445–1514.
16 Y. Xu, Y. Gong, H. Ren, W. Liu, L. Niu, C. Li and X. Liu, *RSC Adv.*, 2017, **7**, 32592–32600.
17 Y. Li, Y. Sun, W. Ho, Y. Zhang, H. Huang, Q. Cai and F. Dong, *Sci. Bull.*, 2018, **63**, 609–620.
18 S. Gu, J. Xie and C. M. Li, *RSC Adv.*, 2014, **4**, 59436–59439.

19 S. Barman and M. Sadhukhan, *J. Mater. Chem.*, 2012, **22**, 21832–21837.
20 M. Ritu, V. K. Tomer, K. Lorenz, C. Vandna, N. Satyapal and D. Surender, *Adv. Mater. Interfaces*, 2018, **5**, 1701357.
21 B. Lin, G. Yang, B. Yang and Y. Zhao, *Appl. Catal., B*, 2016, **198**, 276–285.
22 L. Luo, A. Zhang, M. J. Janik, C. Song and X. Guo, *RSC Adv.*, 2016, **6**, 94496–94501.
23 S. Le, T. Jiang, Y. Li, Q. Zhao, Y. Li, W. Fang and M. Gong, *Appl. Catal., B*, 2017, **200**, 601–610.
24 W.-J. Ong, L.-L. Tan, Y. H. Ng, S.-T. Yong and S.-P. Chai, *Chem. Rev.*, 2016, **116**, 7159–7329.
25 A. Zhang, L. Gu, K. Hou, C. Dai, C. Song and X. Guo, *RSC Adv.*, 2015, **5**, 58355–58362.
26 X. Li, Q. Sun, M. Li, J. Yang, X. Chen, Y. Yang, X. Li, T. Hu, Y. Sui and X. Wu, *Int. J. Mater. Res.*, 2017, **109**, 129–135.
27 J. Cao, C. Qin, Y. Wang, H. Zhang, G. Sun and Z. Zhang, *Materials*, 2017, **10**, 604.
28 L. C. Sim, J. L. Wong, C. H. Hak, J. Y. Tai, K. H. Leong and P. Saravanan, *Beilstein J. Nanotechnol.*, 2018, **9**, 353–363.
29 Y. Bao and K. Chen, *Nano-Micro Lett.*, 2016, **8**, 182–192.
30 D. Gao, Y. Liu, P. Liu, M. Si and D. Xue, *Sci. Rep.*, 2016, **6**, 1–8.
31 S.-Z. Wu, Y.-X. Yu and W.-D. Zhang, *Mater. Sci. Semicond. Process.*, 2014, **24**, 15–20.
32 H. Kim, S. Gim, T. H. Jeon, H. Kim and W. Choi, *ACS Appl. Mater. Interfaces*, 2017, **9**, 40360–40368.
33 H. Wang, X. Zhang, J. Xie, J. Zhang, P. Ma, B. Pan and Y. Xie, *Nanoscale*, 2015, **7**, 5152–5156.
34 B. Choudhury, K. K. Paul, D. Sanyal, A. Hazarika and P. K. Giri, *J. Phys. Chem. C*, 2018, **122**, 9209–9219.
35 M. Zhang, Y. Duan, H. Jia, F. Wang, L. Wang, Z. Su and C. Wang, *Catal. Sci. Technol.*, 2017, **7**, 452–458.
36 J. Zhu, P. Xiao, H. Li and S. A. C. Carabineiro, *ACS Appl. Mater. Interfaces*, 2014, **6**, 16449–16465.
37 H. Katsumata, T. Sakai, T. Suzuki and S. Kaneco, *Ind. Eng. Chem. Res.*, 2014, **53**, 8018–8025.
38 Z. Wang, W. Guan, Y. Sun, F. Dong, Y. Zhou and W.-K. Ho, *Nanoscale*, 2015, **7**, 2471–2479.
39 H. Zhang, L.-H. Guo, L. Zhao, B. Wan and Y. Yang, *J. Phys. Chem. Lett.*, 2015, **6**, 958–963.
40 Y. Wang, S. Zhao, Y. Zhang, W. Chen, S. Yuan, Y. Zhou and Z. Huang, *Appl. Surf. Sci.*, 2019, **463**, 1–8.
41 J. Ding, W. Xu, H. Wan, D. Yuan, C. Chen, L. Wang, G. Guan and W.-L. Dai, *Appl. Catal., B*, 2018, **221**, 626–634.
42 Y. Wei, J. Jiao, Z. Zhao, W. Zhong, J. Li, J. Liu, G. Jiang and A. Duan, *J. Mater. Chem. A*, 2015, **3**, 11074–11085.
43 T. Wang, X. Yan, S. Zhao, B. Lin, C. Xue, G. Yang, S. Ding, B. Yang, C. Ma, G. Yang and G. Yang, *J. Mater. Chem. A*, 2014, **2**, 15611–15619.
44 M. A. Würtele, T. Kolbe, M. Lipsz, A. Külberg, M. Weyers, M. Kneissl and M. Jekel, *Water Res.*, 2011, **45**, 1481–1489.
45 K. Song, M. Mohseni and F. Taghipour, *Water Res.*, 2016, **94**, 341–349.
46 M. A. S. Ibrahim, J. MacAdam, O. Autin and B. Jefferson, *Environ. Technol.*, 2014, **35**, 400–406.
47 G. Palmisano, S. Yurdakal, V. Augugliaro, V. Loddo and L. Palmisano, *Adv. Synth. Catal.*, 2007, **349**, 964–970.
48 S. Yurdakal, G. Palmisano, V. Loddo, V. Augugliaro and L. Palmisano, *J. Am. Chem. Soc.*, 2008, **130**, 1568–1569.
49 V. Augugliaro, V. Loddo, M. J. López-Muñoz, C. Márquez-Álvarez, G. Palmisano, L. Palmisano and S. Yurdakal, *Photochem. Photobiol. Sci.*, 2009, **8**, 663–669.
50 S. Yurdakal and V. Augugliaro, *RSC Adv.*, 2012, **2**, 8375–8380.
51 M. Bellardita, A. Di Paola, B. Megna and L. Palmisano, *Appl. Catal., B*, 2017, **201**, 150–158.
52 A. Di Paola, M. Bellardita, L. Palmisano, Z. Barbieriková and V. Brezová, *J. Photochem. Photobiol., A*, 2014, **273**, 59–67.
53 W. Zhai, S. Xue, A. Zhu, Y. Luo and Y. Tian, *ChemCatChem*, 2010, **3**, 127–130.
54 M. Bellardita, C. Garlisi, A. M. Venezia, G. Palmisano and L. Palmisano, *Catal. Sci. Technol.*, 2018, **8**, 1606–1620.
55 S. Yurdakal, V. Augugliaro, V. Loddo, G. Palmisano and L. Palmisano, *New J. Chem.*, 2012, **36**, 1762–1768.
56 Y. Zhang, Z.-R. Tang, X. Fu and Y.-J. Xu, *ACS Nano*, 2011, **5**, 7426–7435.
57 D. Tsukamoto, M. Ikeda, Y. Shiraishi, T. Hara, N. Ichikuni, S. Tanaka and T. Hirai, *Chem.–Eur. J.*, 2011, **17**, 9816–9824.
58 A. Abd-Elaal, F. Parrino, R. Ciriminna, V. Loddo, L. Palmisano and M. Pagliaro, *ChemistryOpen*, 2015, **4**, 779–785.
59 M. Qamar, R. B. Elsayed, K. R. Alhooshani, M. I. Ahmed and D. W. Bahnemann, *Catal. Commun.*, 2015, **58**, 34–39.
60 M. Qamar, R. B. Elsayed, K. R. Alhooshani, M. I. Ahmed and D. W. Bahnemann, *ACS Appl. Mater. Interfaces*, 2015, **7**, 1257–1269.
61 M. Bellardita, E. I. García-López, G. Marcì, I. Krivtsov, J. R. García and L. Palmisano, *Appl. Catal., B*, 2018, **220**, 222–233.
62 Z. Zhou, K. Li, W. Deng, J. Li, Y. Yan, Y. Li, X. Quan and T. Wang, *J. Hazard. Mater.*, 2020, **387**, 122023.
63 R. A. Fernandes, M. J. Sampaio, E. S. Da Silva, P. Serp, J. L. Faria and C. G. Silva, *Catal. Today*, 2019, **328**, 286–292.
64 M. J. Sampaio, A. Benyounes, P. Serp, J. L. Faria and C. G. Silva, *Appl. Catal., A*, 2018, **551**, 71–78.
65 I. Krivtsov, E. Garcia Lopez, G. Marcì, L. Palmisano, Z. Amghouz, J. R. García, S. Ordóñez and E. Díaz, *Appl. Catal., B*, 2017, **204**, 430–439.
66 M. Kobielusz, P. Mikrut and W. Macyk, Photocatalytic Synthesis of Chemicals, in *Advances in Inorganic Chemistry*, ed. R. van Eldik and W. Macyk, Academic Press, 2018, vol. 72, pp. 93–144.

